

Load-biased martensitic transformation strain of Ti₅₀–Ni₄₇–Co₃ strip obtained by a twin-roll casting technique

L. Isola^a, P. La Roca^a, A. Roatta^a, Ph. Vermaut^b, L. Jordan^b, P. Ochin^c, J. Malarría^{a,*}

^a Instituto de Física Rosario (CONICET-Universidad Nacional de Rosario), Bvrd. 27 de Febrero 210 Bis, S2000EZF Rosario, Argentina

^b Laboratoire de Métallurgie Structurale, Ecole Nationale Supérieure de Chimie de Paris, 11 rue Pierre et Marie Curie, 75231 Paris Cedex 5, France

^c Institut de Chimie et des Matériaux Paris-Est, UMR CNRS 7182, 94320 Thiais, France

ARTICLE INFO

Article history:

Received 15 October 2013

Received in revised form

29 November 2013

Accepted 31 December 2013

Available online 9 January 2014

Keywords:

Ti–Ni alloys

Twin-roll casting

Mechanical properties

Texture

Shape memory alloys

ABSTRACT

Mechanical properties of the Ti₅₀–Ni₄₇–Co₃ (at%) strips produced by twin-roll casting are analyzed, focusing on the maximum recoverable strain obtained by inducing the martensitic transformation under constant tensile load. The recoverable strain achieves a value close to 5.5% for a load of ~120 MPa. The microstructure shows a typical cellular solidification structure, where the austenite grains tend to a columnar array morphology with strong {100}_{B2} fiber texture aligned with ND (perpendicular to the strip surface). On the basis of the measured texture, the maximum B2→B19' transformation strain was estimated at 5.6%, using a Sachs-type upper bound model, which averages the most favorable martensite variants in each grain, disregarding interactions between them. The agreement between the measured maximum recoverable strain and the model's outcome is ascribed to special properties of Ti–Ni alloys, which allow them to overcome incompatibilities in shape changes of transforming grains in this particular polycrystalline environment.

© 2014 Elsevier B.V. All rights reserved.

1. Introduction

Ni–Ti shape memory alloys (SMA) are recognized due to their remarkable functional and physical properties, such as large recoverable strains, corrosion resistance and biocompatibility. This system is nowadays the most widely used in the biomedical field. For some specific applications, the transformation temperatures, hysteresis, and relative stabilities of the phases involved in the underlying martensitic transformation must be modified. This has led to the exploitation of different tools of the physical metallurgy, and in this work we make use of two of them: the addition of a third element and the use of rapid solidification non-conventional production technique.

A small amount of Co is introduced in order to promote the separation of the B2→R and R→B19' transformations, due to a shift of M_s^(B19') downwards lower temperature range [1,2], which is more appropriate for some dental and medical applications [3]. On the other hand, the twin-roll casting (TRC) is a powerful technique, which allows us to obtain semi-finished strips in a one-step procedure directly from the melt. Moreover, a favorable microstructure with a columnar grain morphology and a small grain size can be achieved [4–6].

It is known that the texture plays a very important role in determining the recoverable strains of polycrystalline shape memory

alloys [7]. Rapid solidification produces strong textured columnar grains, where [001]_{B2} is parallel to a normal direction, and then the strip presents a mixture of [100]_{B2} and [110]_{B2} directions, in length and width [8] (directions of type [uv0]_{B2}, distributed between [100]_{B2} and [110]_{B2}, lie parallel to the strip plane). This orientation distribution could mean a priori certain drawback in such polycrystalline aggregate in order to maximize the transformation strain of a Ti–Ni based alloy. Here, it is worth noting that for the B2→B19' transition the maximum value is achieved for the <355>_{B2} directions (above 10%) and directions clustered around, while lower values are obtained for directions spreading between <100>_{B2} and <110>_{B2} (between ~4% and ~9%).

The results reported in the literature remain somewhat controversial: Shu and Bhattacharya [9] evaluated the inner bound of the transformation strain, imposing the same strain on each grain, assuming a strong constraint between neighboring grains. These authors recommend this inner bound as a reasonable estimation of the recoverable transformation strain. Under these hypotheses, the recoverable strain was predicted around 2.3% in Ti–Ni alloys with {001}_{B2} fiber texture.

In Ti–Ni twin-roll strip Goryczka and Ochin [10] reported a recoverable experimental strain of about 3%. Similar values of strain were measured in a Ti–Ni–Co₃ twin-roll strip [11]. In melt spun Ti–Ni ribbons with this texture, Eucken and Hirsch [12] reported that a reversible strain reach 4%. However, most recently [5,13], recoverable strains between 5% and 6% were observed in Ti–Ni–Cu₅ and Ti–Ni meltspun ribbons respectively.

* Corresponding author. Tel.: +54 341 4853200.

E-mail address: malarría@ifir-conicet.gov.ar (J. Malarría).

For additional insights into the factors involved in the recoverable transformation strain in the strong textured Ti–Ni alloys, we analyzed a $\text{Ti}_{50}\text{-Ni}_{47}\text{-Co}_3$ strip produced by twin-roll casting. The recoverable transformation strain measured in load-biased thermal cycling through the martensitic transformation was compared with upper bound of the value predicted by a simple model. This model averages the strains of the constituent grains disregarding their interactions, and taking into account the texture of the rapid solidified strip by introducing the inverse pole figure as a weight function.

2. Experimental set-up

The twin-roll casting consists in the solidification of a melted alloy between two symmetrical rollers, which produces a continuous solid sheet. These rollers rotate at high speed in opposite directions. This system is located in a vacuum chamber in a purified helium atmosphere to protect the material from oxidation and improve thermal conductivity inside the chamber. The melted alloy, placed in a quartz nozzle, is ejected by supplying a pressure of argon, into the nip of the rollers. The processing parameters used in the production of the $\text{Ti}_{50}\text{-Ni}_{47}\text{-Co}_3$ strip are given in Table 1. For detailed description of the twin roll casting procedure applied to Ti–Ni based alloys see Refs. [10,14].

The transformations were characterized by a Mettler DSC 30 differential scanning calorimeter. The electrical resistivity behavior was characterized in a.c. mode, using a generic function generator and a Sr-530 Lock-in amplifier. Strip microstructure was observed using an Olympus PME3 optical microscope and a FEI TECNAI F20 transmission electron microscope (TEM). The specimens were mechanically polished up to 1 μm diamond paste and etched with $1\text{HF} + 4\text{HNO}_3 + 5\text{H}_2\text{O}$ solution for the optical microscope analysis. The thin foils examined in the TEM were prepared with a double jet using 95% acetic acid and 5% perchloric acid. The pole figures were recorded with a Philips X' Pert Pro MPD diffractometer, equipped with a Cu tube, X-ray lens optics, parallel plaques and a graphite monochromator on the outgoing beam and an Eulerian Cradle for texture measurements. Measured pole figures were corrected for defocusing and background and further analyzed by WXpopLA to obtain orientation distribution functions and guarantee pole figure compatibility.

Load-biased thermal cycling was performed in a custom-built machine, which allows us to apply a constant load and program cooling/heating cycles. The machine has an Instron load cell (5 kN) to measure the stress. The strain is measured by an Epsilon 3542 axial extensometer with 10 mm gauge length, clipped between the specimen grips. The sample was cooled with nitrogen vapor, so it was necessary to enclose the sample and the grip in an acrylic cylindrical chamber. Two electrical tubular cartridge heaters inserted into drilled holes of the grip body were used for heating. The system sketch is shown in Fig. 1.

The temperature was measured by a K-thermocouple located in the center of the sample. Besides, the sample was isolated with alumina wool, in order to be cooled and heated by temperature

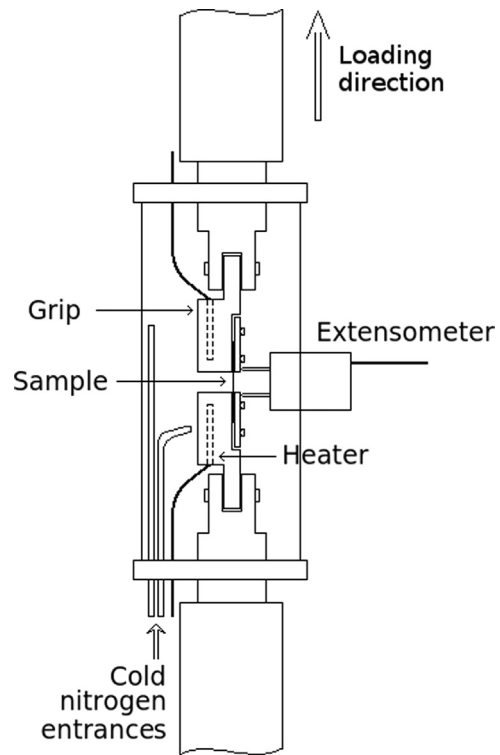


Fig. 1. Thermal cycling load-biased system.

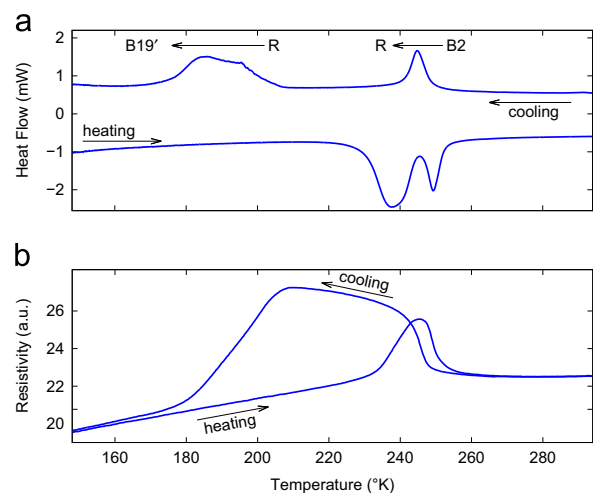


Fig. 2. DSC (a) and resistivity vs. temperature (b), cooling and heating curve of the Ti-NiCo_3 strip.

conduction from the grips, keeping the temperature uniform through the assembly of a lower grip–sample–upper grip.

3. Results

3.1. Thermal-induced transformation and characteristic temperatures

A DSC measure of the as-cast strip is presented in Fig. 2(a). The $\text{Ti}_{50}\text{-Ni}_{47}\text{-Co}_3$ strip undergoes two subsequent martensitic transformations, the first from the B2 parent phase to rhombohedral R-phase and the second transformation between R-phase and monoclinic B19'. The R transformation has small temperature hysteresis

Table 1
Twin-roll casting parameters.

Material	$\text{Ti}_{50}\text{Ni}_{47}\text{Co}_3$
Melt temperature (K)	1783
Roller material	Cu–Co–Be
Rollers speed (m s^{-1})	0.6
Ejection pressure (mbar)	250

5 K and happens near to 248 K, while the transformation to B19' is characterized by a large temperature hysteresis (50 K) and a wide peak in the cooling curve. Goryczka, in Ref. [2], showed that this wide peak is narrowed when successive cycles are performed and it is stabilized after 15 cycles. On heating, we observe two peaks that partially overlap, so that there is no distinct separation for the two corresponding reverse transformations.

The resistivity vs. temperature curve plot is shown in Fig. 2(b). The R-transformation involves a sharp linear increase in resistivity upon cooling and then, by further cooling, a deviation from the initial behavior is compatible with the formation of a third phase with lower electrical resistance, the B19' martensite. Then, the resistivity decreases in the subsequent forward transformation from R-phase to B19'.

On heating, the reverse transformation from B19' to R-phase leads to a strong increase of the electrical resistance, and then, in correspondence with the second DSC peak interval on heating, the strong decrease in the electric signal corresponds to the formation of the parent B2. This is the typical behavior of the Ni–Ti alloys resistivity, where R-phase is present [15,16]. The transformation temperatures are listed in Table 2.

3.2. Microstructural characterization

Fig. 3(a) shows the cross section profile of the strips: the crystallization front proceeds from the surfaces in contact with the wheels, so that transversely elongated grains grow from both sides and joint at an interface revealed by the central axes in the micrograph (see the straight line indicated by an arrow). The directional solidification from the surface towards the strip core originates grains of columnar morphology, whose sizes are of the order of 6–20 μm in section and 100 μm in the elongated direction.

Fig. 3(b) shows the optical image of the surface obtained, after removing a surface layer by polishing. A rather uniform equiaxial grain structure is observed. It means that the columnar grain cross section is of a regular shape.

On a finer scale, TEM observations in samples cut out parallel to the strip surface show a typical cellular solidification structure. These cells can be seen in Fig. 4, they are delineated by precipitates, and they have a characteristic dimension of about 1 μm . In Fig. 4(b), it can be observed that the selected area diffraction patterns do not change significantly across the cell boundaries and confirm them as an internal structure of the columnar grains. These selected area diffraction patterns were obtained moving along a vertical line, where two low angle cell boundaries were observed.

Keeping this in mind, special care must be taken in grain size evaluation, since the actual size of the grains could be underestimated when this is obtained processing optical images, since the chemical etching attacks both the grain and the cell boundaries (see Fig. 3(b)). Because of this in this paper the values for

Table 2

Strip transformation temperatures. The superscripts c and h refer to the cooling and heating curves, respectively.

Measurement technique	R_c^c (K)	R_f^c (K)	M_s (K)	M_f (K)
DSC	249	241	207	174
Resistivity	248	243	207	181
	R_h^h (K)	R_f^h (K)	A_s (K)	A_f (K)
DSC	229	246	246	253
Resistivity	232	245	245	253

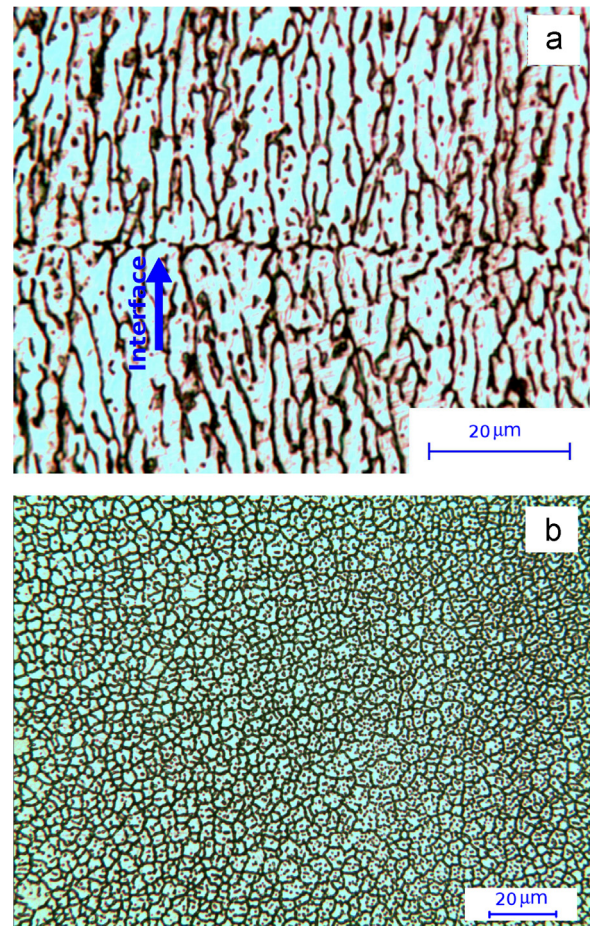


Fig. 3. Optical micrograph of the Ti–Ni–Co₃ strip. Transverse section (a) and surface (b). In (a), the blue arrow indicates the interface between the two solidification fronts. (For interpretation of the references to color in this figure caption, the reader is referred to the web version of this paper.)

grain size were obtained by complementing data from optical and TEM micrographs.

Few dislocations are introduced by the twin roll casting processing route. As can be observed in Fig. 4(a), they are randomly distributed in the grains. The micrograph reveals the presence of precipitates located mainly at the cell boundaries and along the grain boundaries. Many authors reported the presence of the Ti₂Ni precipitates for this kind of strips obtained in the same way. Nevertheless, we consider quite plausible the formation of second phase Ti₄Ni₂O particles as it was pointed out by Dalle et al. [14], who determined oxygen content in twin roll cast Ti₄₂–Ni₅₀–Hf₈ strips. The structures are similar to very close cell parameters. In spite of their rather low volume fraction, these precipitates were identified in the X-ray diffractograms as Ti₄Ni₂O (see Fig. 5).

Fig. 6 shows other microstructural features, a morphological inhomogeneity eventually observed: in some regions, “round islands” are noticed, with a radial structure of fine grains. These “islands” are commonly reported for twin-roll cast strips [11,14], and they should be ascribed to drops of liquid metal embedded in the solid strips that cooled down more slowly and develop a radial structure.

3.3. Texture analysis

To reveal the presence of texture of the Ti₅₀–Ni₄₇–Co₃ strip, the pole figures of {110}_{B2}, {100}_{B2} and {211}_{B2} were measured (Fig. 7). The strong texture in the {100}_{B2} pole figure is typical in the twin-

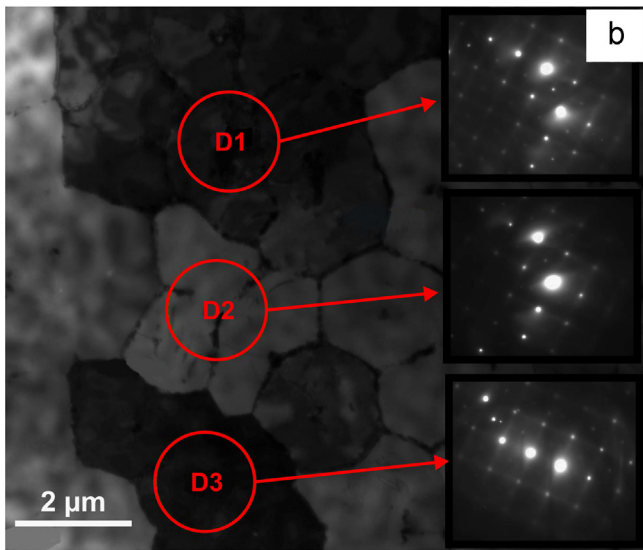
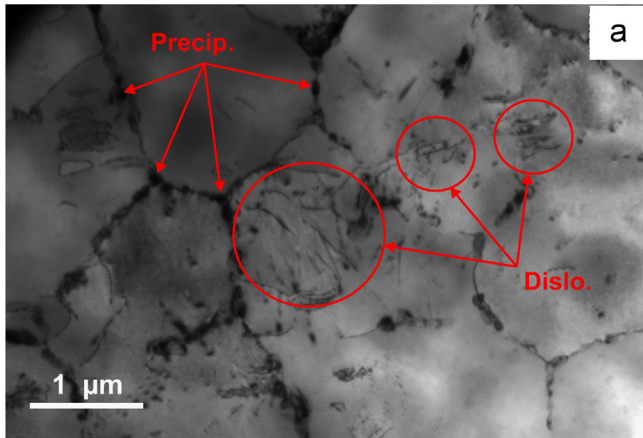


Fig. 4. TEM bright field inside the grains, where it can be seen the dislocations and the precipitates (a) TEM bright field and the corresponding selected area diffraction patterns obtained from a columnar grain of the strip (b).

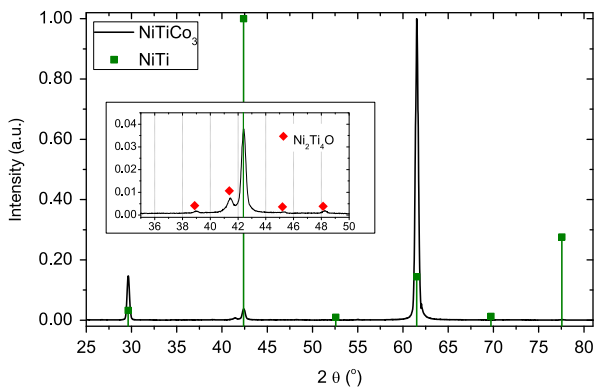


Fig. 5. X-ray diffractogram of the NiTiCo₃ strip. The diffraction peak of the Ti₄Ni₂O precipitates are indicated with ♦.

roll cast strip (a not surprising result if we bear in mind that columnar grains with a preferential axis [100]_{B2} direction parallel to the heat flow are developed in cast of bcc metals; it corresponds also to the most frequently obtained orientation in crystal growth of bcc metal by the Bridgman method). Its maximum normalized intensity is about 40 in a normal direction (ND) to the strip surface. The {110}_{B2} pole figure shows its maximum at $\theta=45^\circ$, and almost random distribution in an azimuthal angle with small

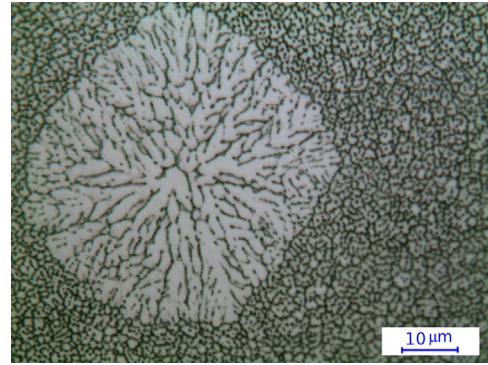


Fig. 6. Optical micrograph of a round island.

local maxima in the rolling (RD) and transverse direction (TD). This means that the B2 cubic structure has a face parallel to the strip surface and an almost random distribution in the directions of the strip plane.

The calculated inverse pole figures are presented in Fig. 8. According to the previous discussion, the inverse pole figure in the rolling direction has almost uniform distribution between [100]_{B2} and [101]_{B2} directions.

3.4. Sachs bound calculation: B2 → B19' transformation strain

The upper bound or the Sachs bound of the recoverable transformation strain is calculated assuming that the most favorable and unique martensite variant grows in each grain to induce maximum deformation [17]. The transformation to the intermediate R-phase is not taken into account since we consider the difference between the final and initial state disregarding any special path. Then, the transformation strain in each grain can be calculated from the lattice distortion due to the martensite transformation and using the lattice constant of the parent and martensite phase. In the calculation, the lattice constant of Ni_{50.7}Ti_{49.3} (235 K) [18] is used: $a_0 = 3.0069(4)\text{Å}$ for the B2 phase and $a = 2.8786(2)\text{Å}$, $b = 4.1340(2)\text{Å}$, $c = 4.6215(4)\text{Å}$ and $\beta = 96.474(8)^\circ$ for the B19' phase.

The lattice distortion matrix T' written in martensite coordinate is [15,17]:

$$T' = \begin{pmatrix} \frac{a}{a_0} & 0 & \frac{c \cos(\beta)}{\sqrt{2}a_0} \\ 0 & \frac{b}{\sqrt{2}a_0} & 0 \\ 0 & 0 & \frac{c \sin(\beta)}{\sqrt{2}a_0} \end{pmatrix} \quad (1)$$

Using the R coordinate transformation matrix from the martensite to the parent phase, the lattice distortion matrix in a parent phase coordinate can be obtained as follows:

$$T = RT'R^t \quad (2)$$

where R^t is the transpose of R . Then, the deformation in any x vector of the B2 phase is transformed to x' through the martensite transformation using:

$$x' = Tx \quad (3)$$

Hence the strain in the direction due to the lattice distortion is

$$\varepsilon = \frac{|x'| - |x|}{|x|} \quad (4)$$

In the cubic to monoclinic transformation, there are 12T symmetry-related variants of martensite, therefore there are 12 symmetry-related lattice distortion matrices. Hence, in order to calculate the maximum strain (ε_M) in each grain, it is necessary to maximize the expression (4) on the 12 martensitic variants. Fig. 9

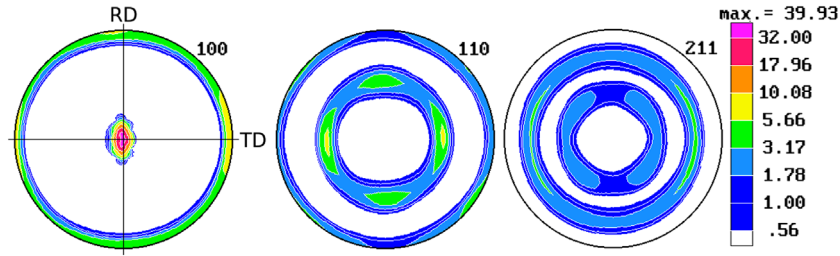


Fig. 7. $\{100\}_{B2}$, $\{110\}_{B2}$ and $\{211\}_{B2}$ pole figure measurements of the TRC strip.

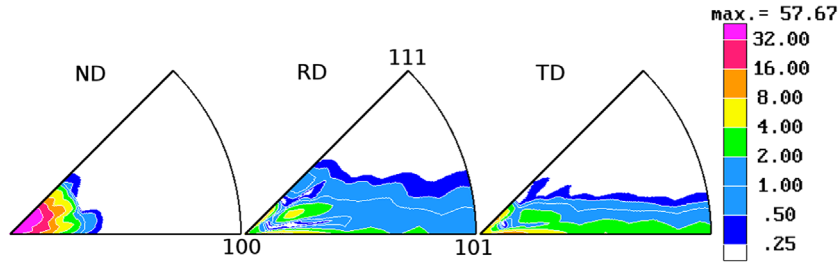


Fig. 8. Inverse pole figures in normal, rolling and transverse directions.

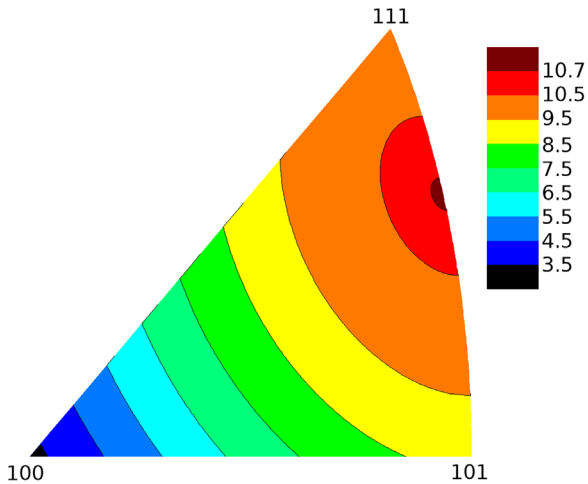


Fig. 9. Maximum transformation strain (ϵ_M) expressed by contour lines on the B2 phase reference system. The maximum value ($> 10\%$) is reached in the $[355]_{B2}$ direction.

shows the ϵ_M for each direction expressed by contour lines in the stereographic triangle.

Finally, the Sachs bound is calculated averaging ϵ_M on the inverse pole intensities (I^i), this can be done with the following expression [17]:

$$\bar{\epsilon}_M = \frac{\sum_{i=1}^N \epsilon_M^i I^i}{\sum_{i=1}^N I^i} \quad (5)$$

where $N=361$ is the number of points in the inverse pole figure used in the calculation in order to take into account the polycrystal texture. Using the rolling direction inverse pole figure reported in Fig. 8, the Sachs bound in the rolling direction is 5.6% for our Ti–Ni–Co₃ twin-roll strip.

From the expression (5) it is straightforward that the Sachs bound uncertainty depends on the inverse pole intensities and lattice parameter uncertainties. In order to estimate the importance of the inverse pole intensity uncertainty, the texture was measured in different places of the strip. In all cases the change in the Sachs bound value was lower than 0.4%. On the other hand, the

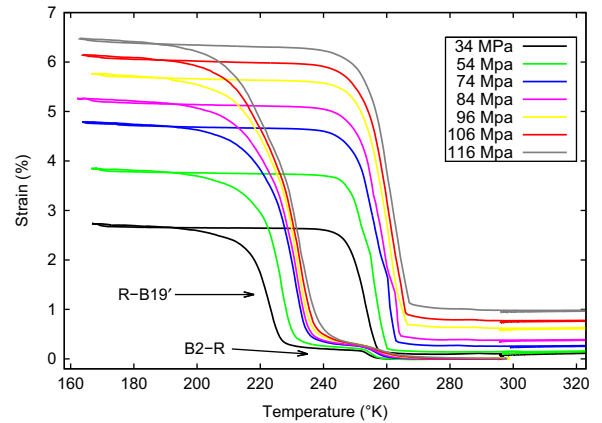


Fig. 10. Strain in the thermal cycling for different tensile stresses.

influence of the lattice parameter uncertainty might be more critical. For instance, if the lattice parameters B2 were 0.01 Å lower, the Sachs bound grows to 5.9%. However, from XRD experiments reported in [19], the 3% Co addition to Ti–Ni modifies the lattice parameters of both phases in less than 0.2%. Therefore, the lattice parameters of Ti–Ni taken from [18] are suitable for our assessment.

3.5. Load-biased thermal cycles

Several thermomechanical series were performed to test the as-cast Ti₅₀–Ni₄₇–Co₃ strip. The external stress was increased up to 120 MPa, setting the load during the hold time at the upper temperature limit for each cycle. Fig. 10 shows the strain loops of the thermal-cycle experiments at different constant tensile load for a representative sample. It can be seen the two transformations between B2 → R and R → B19' in every curve. The former appears as a small elongation in the cooling part at about 255 K and the latter, which is much larger, happens at about 235 K. As expected, an increase of the transformation strain is observed as the applied load raised, since the volume fraction of martensite variants promoted by the external stress increases (these variants are responsible for the macroscopic shape change). Maximum strain exceeds 6%,

however the unrecovered strain is over 0.5% at stress higher than 90 MPa. Also, it is observed that the transformation temperatures rise as tensile stress increases, according to the Clausius–Clapeyron relation [20]. The shift is larger for the R→B19' than for the B2→R due to the differences in the dependence of the transformation temperature on the external stress in each transition [5].

Fig. 11 is a plot of recovered transformation strain as a function of tensile stress. The maximum recoverable strain reaches a value of about 5.5%, close to a saturation regime. This value is fairly close to the Sachs bound limit (5.6%), calculated in previous section, which assumes that each grain transforms as isolated grains regardless of the interaction between them. The measured recoverable transformation strain is in good agreement with the values obtained by Khantachawa et al. [13] and Santamarta et al. [5] on Ti–Ni and Ti–Ni–Cu₅ melt spun ribbons, respectively, with a similar texture.

It should be noted that the strain is recorded with an extensometer clipped directly at the level of the gauge length limits of the specimen, and this provides a highly reliable value for the transformation strain.

Moreover, this experimental set-up allows us to suppress the shift between the cooling and heating branch normally observed in this kind of experiments when the displacement is recorded by means of a LVDT, which is usually fitted to the rod that connect one of the grips to the load frame, or either on sideways. In such a case a shift between the cooling and heating branches is introduced due to temperature gradients between the sensor and the grips-sample assembly, also the thermal expansion record of the involved phases (i.e. the base-line) maybe slightly distorted, and loops are usually observed at the run limits related to a delay in the temperature heating/cooling rate inversion. Our assembly guarantees that the signal recorded by the extensometer corresponds to the actual deformation of the sample, reducing undesired experimental artifacts.

4. Discussion

The closeness between the measured recoverable strain and the Sachs bound is initially a somewhat surprising result. Shu and Bhattacharya [9] indicated that the estimate based on a Taylor bound (i.e. an inner bound obtained by assuming that the strain is recoverable on every constituent grain and continuous on grain boundaries, accounting intergranular constraints) is more compatible with experimental values for many textures. They predict a uniaxial

recoverable extension of 2.3% for ribbons with {100}_{B2} solidification texture. As it has been pointed out, the texture is a very important factor in order to analyze the possible recoverable strain [21,22]. However, to rationalize whether the result approaches the upper (Sachs type) or the inner (Taylor type) bound it is also necessary to consider the particular microstructure and its effect on the grain compatibility.

Regarding the microstructure, compatibility requirements are reduced in the case of columnar grains and a strong texture provides a coherency in the array of grains which can make easier a cooperative accommodation of transforming domains. The columnar grain morphology reduces the grain constraint [8], since the boundary number is reduced through the thickness of the strip. This means a better geometrical correspondence with an idealized array of series connected grains, where the constant stress Sachs approach holds. Although it is far from a bamboo-like array reported for other shape memory alloys [23], the grains have a greater freedom to deform independently in response to the uniform applied stress with no regard to the constraint imposed by its neighbors.

It is worth noting that the grain size produced by TRC (6–20 μm) is large enough to neglect its effect on the macroscopic thermomechanical behavior of Ni–Ti alloys, which appears in 100-nm grains [24]. On the other hand, this grain size produces that the unrecovered strain appears at relatively large loads (it is well known the dependence of yield stress on the grain size [25]).

The other topic to be introduced in the analysis is the particular properties of the underlying martensitic transformation, in order to overcome strain incompatibilities at the grain level.

It is well known that when the polycrystalline body undergoes a martensitic transformation under load, many grains will be oriented favorably and others unfavorably with respect to the applied stress. According to in situ optical microscope observations of Brinson [26] the transformation begins inside isolated grains that are oriented preferentially with respect to the applied stress. Models of Novák and Šittner [27] and Schlomerkemper and Bhattacharya [28] have shown that the Sachs bound correctly predicts the onset of the transformation in a granular polycrystal.

In this frame, when a critical temperature is reached, the martensitic transformation will start in the grains most favorably oriented and the most favored variant will appear and grow in each of them. In a first stage, each grain deforms independently in response to the uniform applied stress with no regard to the constraint imposed by its neighbors. Afterwards, the misorientation will result in unbalanced transformation strain magnitudes for neighboring grains, introducing local stress and strain fields. The transformation is arrested by intergranular constraints and can only proceed by further cooling.

Here is a problem of whether a single martensite variant can finally fill the entire parent grain with increasing deformation. Due to the lack of compatibility, further deformation is realized by nucleation of other variants in the remaining austenite of the grain domain, rearrangements of martensite variants, and also some irrecoverable plastic strain can be introduced by applying an external stress above certain limit.

In order to get a better understanding, it is useful to introduce here Liu's representation of the polycrystalline aggregate in which a finite volume is considered to represent the "grain boundary affected regions" (see Fig. 1 in Ref. [29]), where the compatibility problems must be solved, and the grain interior region, where the martensite variant promoted by the external stress grows in a constrained-reduced environment. The close agreement observed (Fig. 11) between the maximum recoverable strain and the upper limit provided by the Sachs bound indicates that the most favored variant in each grain shares the more volume percent as a whole to the detriment of the grain boundary affected regions.

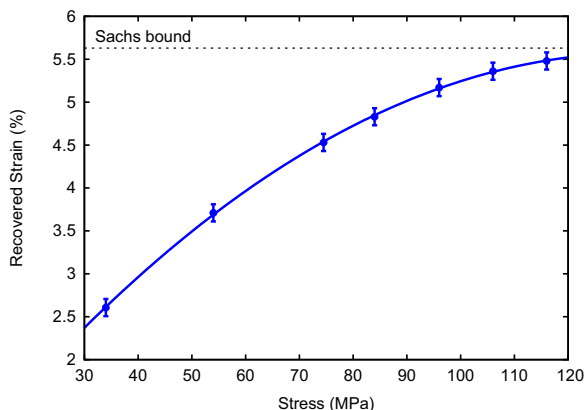


Fig. 11. Recovered strain as a function of load stress in the thermal-cycles.

These may result from the conjunction of many favorable factors, among them the above-mentioned microstructural features. In addition to this, as was highlighted by Bhattacharya and Kohn [21] by analyzing the change of symmetry associated with the transformation, the alloys undergoing cubic to monoclinic structures have greater freedom to rearrange martensite variants reducing damage and irreversible slip at grain boundaries. And among this, Ti–Ni alloys have unique characteristics [30]: the high variety of twinning and reorientation process available in the B19' enables many options for grain boundary mismatch accommodation. As much as in an intermediate step a twinning correlated martensite pair can be easily formed reducing local stresses at grain boundaries, then the detwinning process seems to be no difficult.

Another contribution to overcome the lack of strain compatibilities is provided by the elastic and transformation anisotropies of Ti–Ni in tension mode, which tend to compensate each other: although the grains oriented in the $\langle 100 \rangle_{B2}$ directions are relatively “hard to transform” grains, they are capable of accommodating large strains elastically due to their smallest Young's modulus (Fig. 8 in Ref. [31] provides a very illustrative representation of the elastic and transformation anisotropies). Moreover, although the $\langle 100 \rangle_{B2}$ oriented grains remain elastic in early stages of transformation, and transform at relatively higher stresses compared to $\langle 110 \rangle_{B2}$, their proportion is rather low since the orientations are nearly evenly spread between $[100]_{B2}$ and $[101]_{B2}$ (Fig. 8). Such a compensation mechanism could be just operative in this polycrystalline array with $\{100\}_{B2}$ solidification texture.

An alternative option to accommodate a mismatch for a “hard to transform” grain is the intermediate cubic to trigonal transformation to the R-phase (responsible for the separate stages of yielding in the thermal transformations under constant load shown in Fig. 10). The transformation to the R-phase is highly thermoelastic, involving reduced values of stress and hysteresis. Sittner et al. [32] investigated the B2 to R-phase by *in situ* neutron diffraction, and suggested that the apparent elastic modulus significantly decreases from 70 to 20 GPa, when the R-phase transformation proceeds. The R phase can easily be nucleated and could act as a local soft buffer that smooths adverse misfit of adjacent grains.

In short, through the arguments presented in this section we attempt to emphasize that, due to the conjunction of the resources of Ti–Ni SMA to accommodate strain mismatch and a suitable texture and microstructure morphology of columnar grains, Ti–Ni alloys are able to fix compatibility problems in a relative confined space. And, in view of the closeness of the experimental recoverable transformation and the Sachs bound, the variant promoted by the external stress nearly covers every parent grain.

We finally comment on the potential applications of these Ti–Ni–Co strips as linear actuators. In the selection and tailoring of Ti–Ni SMA for actuators the introduction of a fiber $\langle 111 \rangle_{B2}$ in the action line is pursued to maximize the transformation strain. This kind of textures is common in Ti–Ni drawn bars [33,34] and wires [35]. Miyazaki observed a recoverable strain of nearly 6% for drawn wires [36], and values among 4% and 6% are reported in the literature [37–40]. The recoverable strain presented in this paper for the strips obtained by twin roll casting achieves a value of about 5.5%, i.e. same order of the values reported for drawn wires. So, in spite of their a priori not suitable $\{100\}_{B2}$ solidification texture derived from the elaboration procedure, these strips look promising as an active part of SMA actuators, mainly where flat specimens are needed. The elaboration procedure is rather complex, but near final-shape actuators can be obtained in one single step, avoiding rolling (or drawing)-recovery stages and additional thermomechanical treatments needed in conventional cast alloys. The precipitates introduced in the manufacturing process seem not to suppress nor hinder the growth and rearrange of martensite phase. On the other hand, they are effective in strengthening the material since nearly

closed loops are obtained indeed by applying loads of about 100 MPa.

5. Summary and conclusion

Ti₅₀–Ni₄₇–Co₃ strips obtained by the twin roll casting process show a typical solidification structure, where austenite columnar grains tend to be oriented perpendicular to the strip surfaces (in the sense of the solidification direction). The high cooling rate leads to a solidification texture where the axial $[001]_{B2}$ is clearly dominant.

The degree of shape recovery reaches a value of about 5.5% in thermal cycling under load experiments. Using data of measured inverse pole figures as weight function, we performed the calculation of the Sachs type upper bound, where it is assumed that the most favorable and unique martensite variant grows in each grain, disregarding the interactions between neighboring grains. The outcome of this idealization leads to a transformation strain of 5.6%, slightly above the experimental value of nearly 5.5%.

Although having $\{001\}_{B2}$ solidification texture means that there are no variants with the maximum deformation completely aligned in the direction of the applied stress, the maximum reversible transformation strain is close to the most optimistic limit. Moreover, the value is comparable with the result reported in the literature for other Ti–Ni based polycrystals with a priori more favorable textures. The results show that strips obtained by twin roll casting could be considered as a good option for flat actuators.

Acknowledgments

The authors would like to thank Daniel Castelani for this valuable collaboration in the development of the instrumentation. They express grateful acknowledgment to Conicet (Argentina), financial support from the “Agencia Nacional de Promoción Científica y Tecnológica”, Argentina (under Grant PICT 2140) and ECOS program (project no. A10E02).

References

- [1] P. Vermaut, M. Lamicol, M. Hytch, P. Ochin, R. Portier, *J. Phys. IV Fr.* 11 (2001) 451–456.
- [2] T. Goryczka, *Mater. Sci. Eng.: A* 481–482 (2008) 676–679.
- [3] L. Jordan, M. Masse, A. Villafana, G. Bouquet, in: Proceedings of the International Conference on Martensitic Transformation, ICOMAT 92, Monterey Institute for Advanced Studies, USA, 1993, pp. 635–640.
- [4] J.V. Wood, P.H. Shingu, *Metall. Trans. A* 15 (1984) 471–480.
- [5] R. Santamarta, E. Cesari, J. Pons, T. Goryczka, *Metall. Mater. Trans. A* 35 (2004) 761–770.
- [6] P. Ochin, A. Dezellus, P. Plaindoux, P. Vermaut, F. Dalle, R. Portier, *J. Phys. IV Fr.* 112 (2003) 881–884.
- [7] C. Sobrero, P. La Roca, A. Roatta, R. Bolmaro, J. Malarria, *Mater. Sci. Eng.: A* 536 (2012) 207–215.
- [8] S. Eucken, J. Hirsch, E. Hornbogen, *Textures Microstruct.* 8 & 9 (1988) 415–426.
- [9] Y.C. Shu, K. Bhattacharya, *Acta Mater.* 46 (1998) 5457–5473.
- [10] T. Goryczka, P. Ochin, *J. Mater. Process. Technol.* 162–163 (2005) 178–183.
- [11] T. Goryczka, *Solid State Phenom.* 154 (2009) 59–64.
- [12] S. Eucken, J. Hirsch, *Mater. Sci. Forum* 56–58 (1990) 487–492.
- [13] A. Khantachawana, H. Mizubayashi, S. Miyazaki, *Mater. Trans.* 45 (2004) 214–218.
- [14] F. Dalle, G. Despert, R. Portier, A. Dezellus, P. Plaindoux, P. Ochin, *Mater. Sci. Eng. A* 346 (2003) 320–327.
- [15] K. Otsuka, X. Ren, *Progr. Mater. Sci.* 50 (2005) 511–678.
- [16] J. Olbricht, A. Yawny, J.L. Pelegrina, A. Dlouhy, G. Eggeler, *Mater. Sci. Eng.: A* 42 (2011) 2556–2574.
- [17] S. Miyazaki, V.H. No, K. Kitamura, A. Khantachawana, H. Hosoda, *Int. J. Plast.* 16 (2000) 4–8.
- [18] J. Khalil-Allafi, W. Schmahl, M. Wagner, H. Sitepu, D. Toebbens, G. Eggeler, *Mater. Sci. Eng.: A* 378 (2004) 161–164.
- [19] L. Jordan, *Evolutions structurales d'alliages a memoire de forme NiTi et NiTiCo destines a l'odontologie* (Ph.D. thesis), Universite de Paris VII, Faculte de Chirurgie Dentaire, 1993.
- [20] P. Wollants, M. De Bonte, J. Roos, *Z. Metall.* 70 (1979) 113–117.

- [21] K. Bhattacharya, R. Kohn, *Acta Mater.* 44 (1996) 529–542.
- [22] W. Yuan, S. Yi, *Mater. Sci. Eng.: A* 271 (1999) 439–448.
- [23] Y. Sutou, T. Omori, J. Wang, R. Kainuma, K. Ishida, *Mater. Sci. Eng.: A* 378 (2004) 278–282.
- [24] T. Waitz, T. Antretter, F.D. Fischer, H.P. Karnthaler, *Mater. Sci. Technol.* 24 (2008) 934–940.
- [25] T. Sawaguchi, M. Sato, A. Ishida, *Metall. Mater. Trans. A* 35 (2004) 111–119.
- [26] L. Brinson, *J. Mech. Phys. Solids* 52 (2004) 1549–1571.
- [27] P. Šittner, V. Novák, *Int. J. Plast.* 16 (2000) 1243–1268.
- [28] A. Schlömerkemper, K. Bhattacharya, *Proc. Appl. Math. Mech.* 8 (8) (2008) 10569–10570.
- [29] Y. Liu, D. Favier, L. Orgeas, *Smart Mater. Struct.* 14 (2005) S207–S210.
- [30] K. Otsuka, A. Saxena, J. Deng, X. Ren, *Philos. Mag.* 91 (2011) 4514–4535.
- [31] P. Šittner, Y. Liu, V. Novák, *J. Mech. Phys. Solids* 53 (2005) 1719–1746.
- [32] P. Šittner, P. Lukáš, V. Novák, M.R. Daymond, G.M. Swallowe, *Mater. Sci. Eng. A* 378 (2004) 97–104.
- [33] P. Šittner, D. Neov, P. Lukas, D. Toebbens, *J. Neutron Res.* 12 (2004) 15–20.
- [34] K. Yamauchi, M. Nishida, I. Itai, K. Kitamura, A. Chiba, *Mater. Trans. JIM* 37 (1996) 210–217.
- [35] A. Condó, F. Lovey, J. Olbricht, C. Somsen, A. Yawny, *Mater. Sci. Eng.: A* 481–482 (2008) 138–141.
- [36] S. Miyazaki, K. Otsuka, Y. Suzuki, *Scr. Metall.* 15 (1981) 287–292.
- [37] C.J. Araújo, M. Morin, G. Guénin, *J. Phys. IV Fr.* 7 (1997) 501–506.
- [38] E. López Cuéllar, G. Guénin, M. Morin, *Mater. Sci. Eng. A* 378 (2004) 115–118.
- [39] R. Matsui, H. Tobushi, T. Ikawa. *Proceedings of The Institution of Mechanical Engineers Part L-journal of Materials-design and Applications - PROC INST MECH ENG L-J MATER.* 01/2004; 218(4):343-353.
- [40] V. Novák, P. Šittner, G.N. Dayananda, F.M. Braz-Frenandes, K.K. Mahesh, *Mater. Sci. Eng. A* 481–482 (2008) 127–133.